Ceramics International 49 (2023) 9725–9734

Contents lists available at ScienceDirect

Ceramics International

journal homepage: www.elsevier.com/locate/ceramint

Portland cement clinkers turned into garnets by spark plasma sintering

José Sanchez del Río [a,b,c], Alicia Páez-Pavón [d], José M. Torralba [c,e,**], Dariusz Garbiec [f], José S. Moya [g], Sonia Lopez-Esteban [h,*], Carlos Pecharroman [h]

[a] E.T.S. of Design and Industrial Engineering (E.T.S.I.D.I), Department of Electrical, Electronics, Automation Engineering and Applied Physics, Universidad Politécnica de Madrid, C/Ronda de Valencia, 3, 28012, Madrid, Spain
[b] Institute for Research in Technology, ICAI School of Engineering, Pontifical Comillas University, C/Santa Cruz de Marcenado, 26, 28015 Madrid, Spain
[c] IMDEA Materials Institute, c/ Eric Kandel 2, 28906 Getafe, Madrid, Spain
[d] School of Architecture, Engineering and Design, Universidad Europea De Madrid, C/Tajo s/n, 28670, Villaviciosa De Odón, Spain
[e] Universidad Carlos III de Madrid, Av. De la Universidad 30, 28911, Leganés, Spain
[f] Łukasiewicz Research Network – Poznań Institute of Technology, 6 Ewarysta Estkowskiego St., 61-755, Poznan, Poland
[g] Nanomaterials and Nanotechnology Research Center (CINN-CSIC), Universidad de Oviedo (UO), Principado de Asturias (PA), Avda. de la Vega, 4-6, El Entrego, 33940, Spain
[h] Instituto de Ciencia de Materiales de Madrid (ICMM), Consejo Superior de Investigaciones Científicas (CSIC), C/ Sor Juana Inés de la Cruz, 3, Madrid, 28049, Spain

ARTICLE INFO

Keywords:
Portland cement clinker
Garnet
Spark plasma sintering (SPS)
Microstructure

ABSTRACT

The feasibility of sintering Portland cement clinker powders by Spark Plasma Sintering (SPS) has been studied. Different SPSed compacts have been successfully obtained by this technique. The compacts have been characterized by means of X-Ray Diffraction, InfraRed spectroscopy, Scanning Electron Microscopy, Raman Microscopy and Vickers hardness. It is worth noting the finding that slight mineralogical variations in the starting compositions may induce dramatic changes, both in the final mineralogical composition and in the morphology, which can affect the properties of the SPSed compacts. Thus, we find that SPS allows artificial garnets to be obtained in the laboratory by applying pressures as low as 50 MPa, while they are materials that would require much higher pressures in natural environments (2–10 GPa). According to the Selsing model, it has been calculated that the material itself acts as a pressure amplifier at the micrometric level by a factor of 40–200 times. A new model describing the formation of garnets considering the emergence of two transitory eutectic liquids has been explained to justify this phenomenon. This result opens the door to looking for compositions for specific applications with high added value in the field (i.e. high hardness), mainly in the manufacturing of high-pressure (GPa) phases by applying relatively low pressures (MPa).

1. Introduction

From a chemical point of view, Portland clinkers can be considered as mixtures of tricalcium silicate ($3CaO{\cdot}SiO_2$, i.e., C_3S), dicalcium silicate ($2CaO{\cdot}SiO_2$, i.e., C_2S), small amounts of tricalcium aluminate ($3CaO{\cdot}Al_2O_3$, i.e., C_3A), calcium alumina-ferrites ($4CaO{\cdot}Al_2O_3{\cdot}Fe_2O_3$, i.e., C_4AF) plus some other mineralogical species such as limestone, gypsum, etc. The main components are C_3S (50–55%) followed by C_2S (19–24%). The addition of different oxides, such as Fe_2O_3, Al_2O_3, MgO, BaO, etc., stabilizes the C_3S phases after quenching. Once calcined, Portland clinkers become concrete by a series of different hydration processes of silicates and aluminates, topic about which a very large volume of scientific and technical reports have been published over the years [1–8].

However, manufacturing dense ceramics from Portland clinkers has not been stated in the scientific literature except for a few works in the 90's [9–13]. The main component of clinkers is C_3S, known as *hartrurite* in its crystalline phase, which may appear as seven different polymorphs [14] with very different specific volumes. For this reason, this phase is very difficult to sinter by pressureless techniques, which prevents the manufacturing of sintered bodies [15]. In this sense, there is no abundant literature about sintered clinkers [16]. Conversely, wollastonite or other calcium monosilicate compounds have been successfully sintered and are currently employed as biomaterials [17–19].

* Corresponding author. Instituto de Ciencia de Materiales de Madrid (ICMM-CSIC), C/ Sor Juana Inés de La Cruz, 3, Madrid, 28049, Spain.
** Corresponding author. IMDEA Materials Institute, c/ Eric Kandel 2, 28906 Getafe, Madrid, Spain.
E-mail addresses: torralba@ing.uc3m.es (J.M. Torralba), s.lopez.esteban@csic.es (S. Lopez-Esteban).

https://doi.org/10.1016/j.ceramint.2022.11.146
Received 4 September 2022; Received in revised form 7 November 2022; Accepted 10 November 2022
Available online 14 November 2022

In order to avoid the difficulties related to the sintering of lime-rich silicates, we have used the Spark Plasma Sintering (SPS) technique. SPS is a relatively new sintering method that employs high electric current pulses with low pressures and allows the achievement of dense bodies in minutes [20–24]. Moreover, it allows obtaining dense compacts from powdered systems that are difficult to sinter by conventional techniques. Due to the extremely fast heating and cooling processes, the sintered bodies are totally out of thermodynamic equilibrium.

The aim of this work is to study the feasibility of sintering Portland cement clinker powders by Spark Plasma Sintering starting from different formulations of powders. All the ceramics have been characterized by multiple techniques to determine their different microstructural features.

2. Materials and methods

2.1. Starting materials

The chemical and mineralogical compositions of ordinary Portland clinker powders used to obtain the SPSed compacts are listed in Table 1. They were provided by the *Official Laboratory for Testing of Construction Materials* (LOEMCO, Getafe, Madrid, Spain).

2.2. Spark plasma sintering

The powders were consolidated by Spark Plasma Sintering (SPS) using a HP D 25/3 furnace (*FCT Systeme GmbH, Germany*) in a 20 mm cylindrical die at 1400 °C, using a heating rate of 100 °C/min from room temperature. The holding time was 15 min And the compaction pressure was 50 MPa. The selection of these SPS conditions was made after an optimization process by testing different conditions with the main goal of achieving the highest density of the compacts.

2.3. Densities

The bulk densities of the obtained samples were determined using the Archimedes method by immersion in distilled water. The relative densities were calculated from the theoretical values according to the following formula [25]:

$$RD\ (\%) = 100 / \Sigma\ \omega_i \cdot \rho_i \quad (1)$$

where ω_i is the mass fraction of each component, and ρ_i is the theoretical density of each component. For this estimation, we have taken into consideration the four main components of each clinker (C_3S, C_2S, C_3A and C_4AF).

2.4. Vickers hardness

The Vickers hardness of the polished surfaces was determined using a *Buehler Micromet 5103* Microindentation Hardness Tester.

2.5. FESEM-EDX and optical microscopy

The fresh fracture surface morphology of the samples was studied by Field Emission Scanning Electron Microscopy at ultra-high resolution with Energy Dispersive X-ray spectroscopy (FESEM-EDX), with a *FEI NOVA NanoSEM* 230 FE-*SEM* (Eindhoven, Netherlands) operating at a maximum voltage of 30 kV. A semi-quantitative analysis of elements was accomplished with the *Apollo 10* EDAX detector (Leicester, UK).

The samples were embedded in resin. The cross-sections were polished down to 1 μm for microscopy study using an optical *Leica DMRM* microscope (Cambridge, UK).

2.6. X-ray diffraction

A *Bruker D8 Advance A25* X-Ray Diffractometer (XRD) with Cu Kα and a PSD-XE with positive discrimination (DAVINCI) was used to characterize both the powder samples and the sintered samples.

2.7. Infrared spectroscopy

Infrared (IR) spectroscopy on powdered and sintered samples was carried out with a *Bruker Vertex* 70V spectrophotometer from 200 μm to 2 μm (50–5000 cm^{-1}). In the case of the powders, conventional transmittance spectra of particles dispersed into a cesium iodide matrix were taken. However, for sintered and polished samples, reflectance spectra were taken using a near-normal reflectance attachment. By a Kramers-Krönig transformation, the reflectance phase was obtained to then, using the Fresnel equations, calculate the complex refractive index. In order to simulate the cesium iodide-powder spectra, the effective medium theory has been used as described in the literature [26–30].

2.8. Raman spectroscopy

Raman experiments have been performed at room temperature with a portable *Raman* analyser (EZ-Raman-N, Enwave Optronics, *USA)*, coupled to an optical *microscope (*Leica DM300) with an Nd:YAG (532 nm) laser.

3. Results

3.1. X-ray diffraction

The X-ray powder diffraction data analyzed by using the *Rietveld* method resulted in the crystalline *mineralogical composition* of the samples as shown in Table 1. Samples have been labelled with ordinal numbers (from 1 to 4) according to the total amount of C_3S, in decreasing order.

Fig. 1 shows the diffractograms of the starting powders and the sintered compacts. Samples S1 and S2 in powder form presented the maxima corresponding to C_3S stronger than those in sintered bodies. As the diffraction patterns were not normalized, the observed peak lowering is even more significant when we consider that the atomic density in the powder state is around half of that of the sintered body. The origin of such a reduction of crystalline phases in samples S1 and S2 can be linked with the appearance of a background at lower angles in the diffractograms, suggesting the presence of large amounts of a glassy phase. Additionally, the intensity of the peaks of the secondary compound, C_2S, has largely decreased in sintered samples. Furthermore, all the minor components, such as aluminates (C_3A, C_4AF), lime and gypsum, nearly vanish.

However, the most striking feature of these two SPSed samples is the

Table 1
Mineralogical and chemical composition of the clinkers.

	Mineralogical composition (wt. %)				Chemical composition (wt. %)					
	C_3S	C_2S	C_3A	C_4AF	CaO	SiO_2	Al_2O_3	Fe_2O_3	MgO	Free CaO
S1	67.60	14.30	7.45	8.64	66.32	20.3	4.62	2.84	1.56	0.96
S2	65.29	17.54	10.61	0.94	67.09	23.29	4.20	0.31	0.81	0.51
S3	59.38	16.17	6.81	11.60	65.18	21.26	5.00	3.81	1.37	1.29
S4	55.72	21.04	3.95	12.19	66.85	22.00	4.05	4.01	1.69	0.99

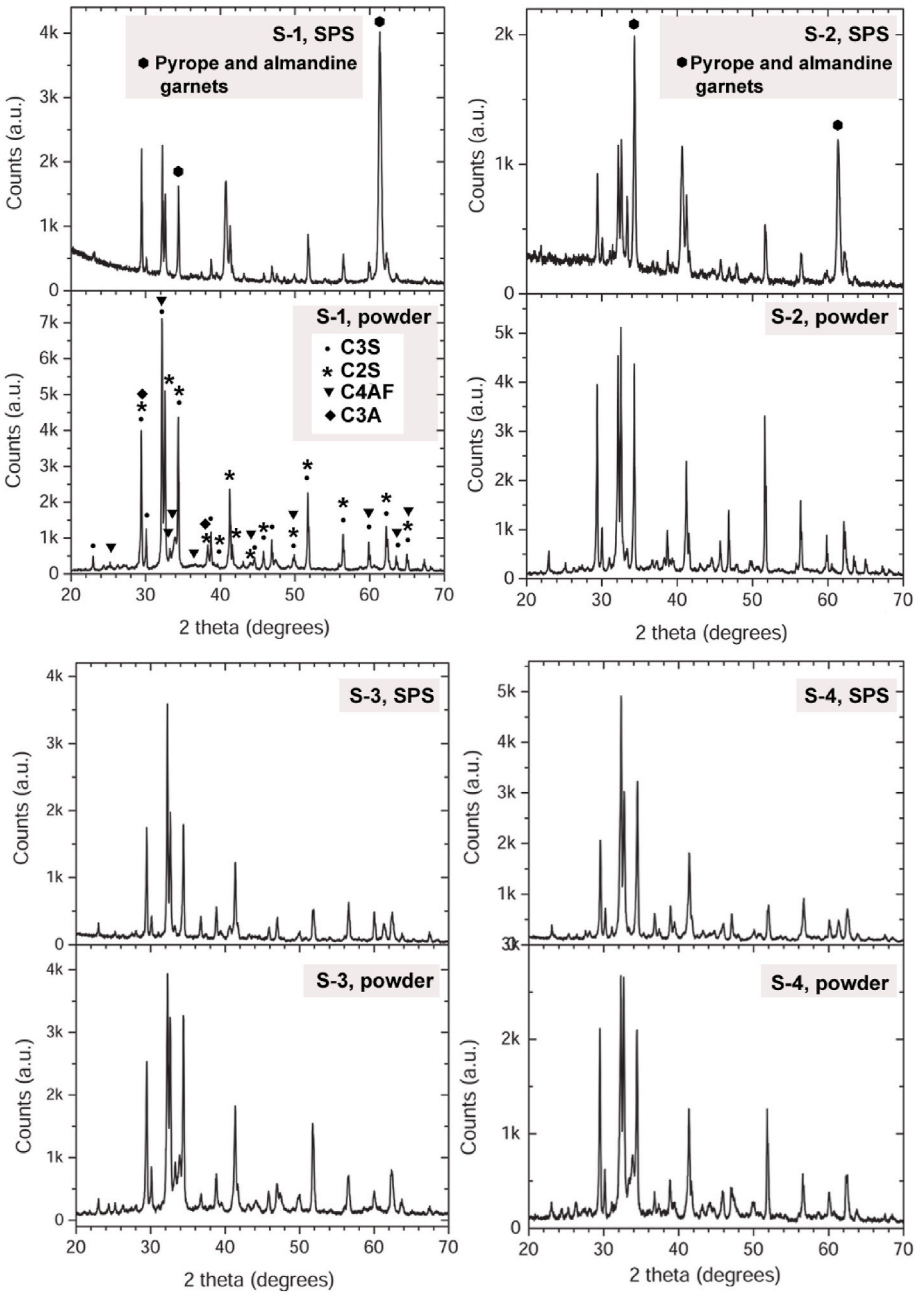

Fig. 1. XRD diffractograms of the powder and SPSed samples. In the diffractograms of the SPSed samples S1 and S2, the main peaks of garnets pyrope and almandine have been indicated.

strong peak around $2\theta = 61°$. As the intensity of the x-ray diffraction peak reduces at high angles due to the profile of the radial atomic electron, this feature becomes a unique fingerprint, which points to the presence of an unusual substance. In this case, the better fit corresponds to the (642) plane of garnet crystals. Silica-based garnets [31] are substances with a chemical composition of $X_3Y_2(SiO_4)_3$, where X^{2+} and Y^{3+} are respectively divalent and trivalent cations, which are often used as gemstones, hard materials, and are key minerals to determine the nature of the geological process of rocks. Depending on the type of the X^{2+} and Y^{3+} cations, different minerals can be distinguished, although it is very common to find solid solutions with divalent and trivalent cations together [32–34]. The most likely compositions in this case, which fit better with the high angle strong peaks in samples S1 and S2, could be almandine ($Fe_3Al_2(SiO_4)_3$), pyrope ($Mg_3Al_2(SiO_4)_3$), or a solid solution of both. The presence in the sintered compacts of Fe^{2+} instead of the Fe^{3+} of the precursor would be a direct consequence of the SPS reducing conditions.

The diffractograms of sintered samples S3 and S4 do not present large backgrounds corresponding to an amorphous phase. Instead, their XRD patterns look similar to those of powders of S1 and S2, with the exception of the elimination of some small peaks corresponding to lime or gypsum. Anecdotally, the presence of small peaks corresponding to garnets is also visible.

3.2. *Infrared spectroscopy*

Large area infrared spectra complement the XRD information because nanocrystals or even amorphous structures present a strong electromagnetic response at the IR wavelengths. As IR spectroscopy is sensitive to the dipolar momentum, it can excite both local and

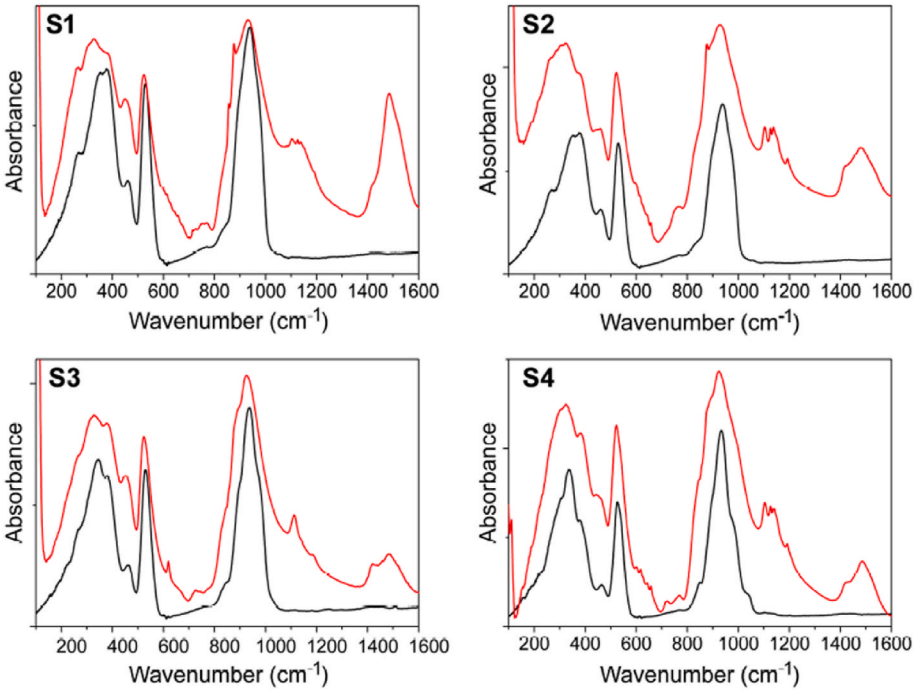

Fig. 2. IR spectra of samples S1, S2, S3 and S4. Red lines (the one above for each sample) stand for powder absorbance of non-sintered clinker powders dispersed into a CsI matrix. Equivalent absorbance of the four sintered samples appear as black lines (the one below for each sample). These spectra were calculated from Kramers-Krönig transformations on specular reflectance on polished sintered samples. (For interpretation of the references to color in this figure legend, the reader is referred to the Web version of this article.)

collective vibrations, so that large-range order at the analyzed samples is not a requirement for this technique. The collected spectra appear in Fig. 2 where we have employed conventional absorbance of dispersed powder and near-normal reflectance for sintered bodies. In order to compare both sets of data, a Kramers-Krönig transformation was carried out on reflectance spectra to obtain the phase. Using Fresnel equations, it was possible to determine the dielectric constant, which was modeled by an effective medium model [29,30] to simulate the absorption spectra of powder in cesium iodide.

The spectra of precursors present features at specific wavelength ranges, defining families of modes, at diverse spectral ranges corresponding to different atomic groups. From higher to lower wavenumbers, they can be classified as follows: (a) modes from 1400 to 1500 cm^{-1} are CO_3^{2-} stretching vibrations (mostly, from calcium and magnesium carbonates); (b) around 1100 cm^{-1} appear the IR activity of different salts of hydrated calcium sulphate (gypsum); (c) from 800 to 1050 cm^{-1} the characteristic symmetrical and antisymmetrical stretching modes of SiO_4 tetrahedral appear.

According to published references [35–37], small peaks seem to be associated with C_2S while broad shoulders match with C_3S modes. Such a difference seems to indicate that C_2S particles have a higher degree of crystallinity, while the space correlation length of C_3S is quite small. At lower frequencies, from 700 to 800 cm^{-1}, one can see the stretching modes of aluminates. Finally, below 600 cm^{-1}, IR modes are due to metallic cation vibrations. It should be pointed out that, for experimental reasons, all the references found do not show frequencies below 400 cm^{-1} [35,36].

As shown in Fig. 2, the spectra of sintered bodies are definitely different from those of powders. Firstly, for sintered samples, neither carbonates nor sulfates appear, as those compounds decompose at relatively low temperatures. Additionally, aluminate bands nearly vanish, which suggests that Al^{3+} cations entered into a solid solution of silicate. In S1 and S2, no sharp peaks appear at the Si–O stretching region, which suggests an amorphous structure for this silicate, and the small contribution of C_2S has totally disappeared. On the other hand, S3 and S4 display similar spectral features to those of powdered samples.

3.3. FE-SEM

Fig. 3 shows FE-SEM images of the polished surfaces and fracture surfaces of the four sintered samples. Regarding polished samples, S1 and S2 display smoother surfaces than S3 and S4. This fact could be due to the large amount of glassy phase in S1 and S2, while polishing in samples S3 and S4 induces pulling-out grains. Regarding the fracture surfaces, S1 and S2 present a uniform, smooth and clean fracture surface with few sharp edges, corresponding to a transgranular fracture. On the contrary, in S3 and S4, the fracture surface is much steeper, with large irregularities corresponding to an intergranular fracture. The composition of the clinkers, therefore, involves a change in the behavior in the fracture mechanism. Their appearance seems to be related to a microstructure softening, becoming more homogeneous.

3.4. Densities

The shrinkage of the sintered powders was analyzed based on the punch displacement dependences on the holding time and is shown in Fig. 4. It is seen that densification of S1, S2, S3 and S4 powder is completed under certain conditions. The plateau of the sintering curves is clearly seen for S1, S3 and S4 after ≈9–11 min holding time. For S2 powder, the plateau was achieved after ≈14 min 40 s holding time. According to Table 2, the measured densities of the four clinkers are similar, while the relative densities decrease significantly with C_3S content. Thus, this decrease in hardness may be related to the decrease in density. However, it is worth noting that the highest Vickers hardness values correspond to S1 and S2, which are the compacts that present garnets in their microstructure (manifest by a strong peak at 61° in the X-Ray diffractograms), and the hardness of the garnets reaches really high values in the range of 13–15 GPa [38]. Thus, as the C_3S content decreases, the relative densities decrease, as well as the amount of garnets (according to XRD), and both factors may contribute to the decrease in the final hardness of the compacts.

3.5. Optical microscopy and FESEM-EDX

In order to detect the presence of garnets, we have taken into account

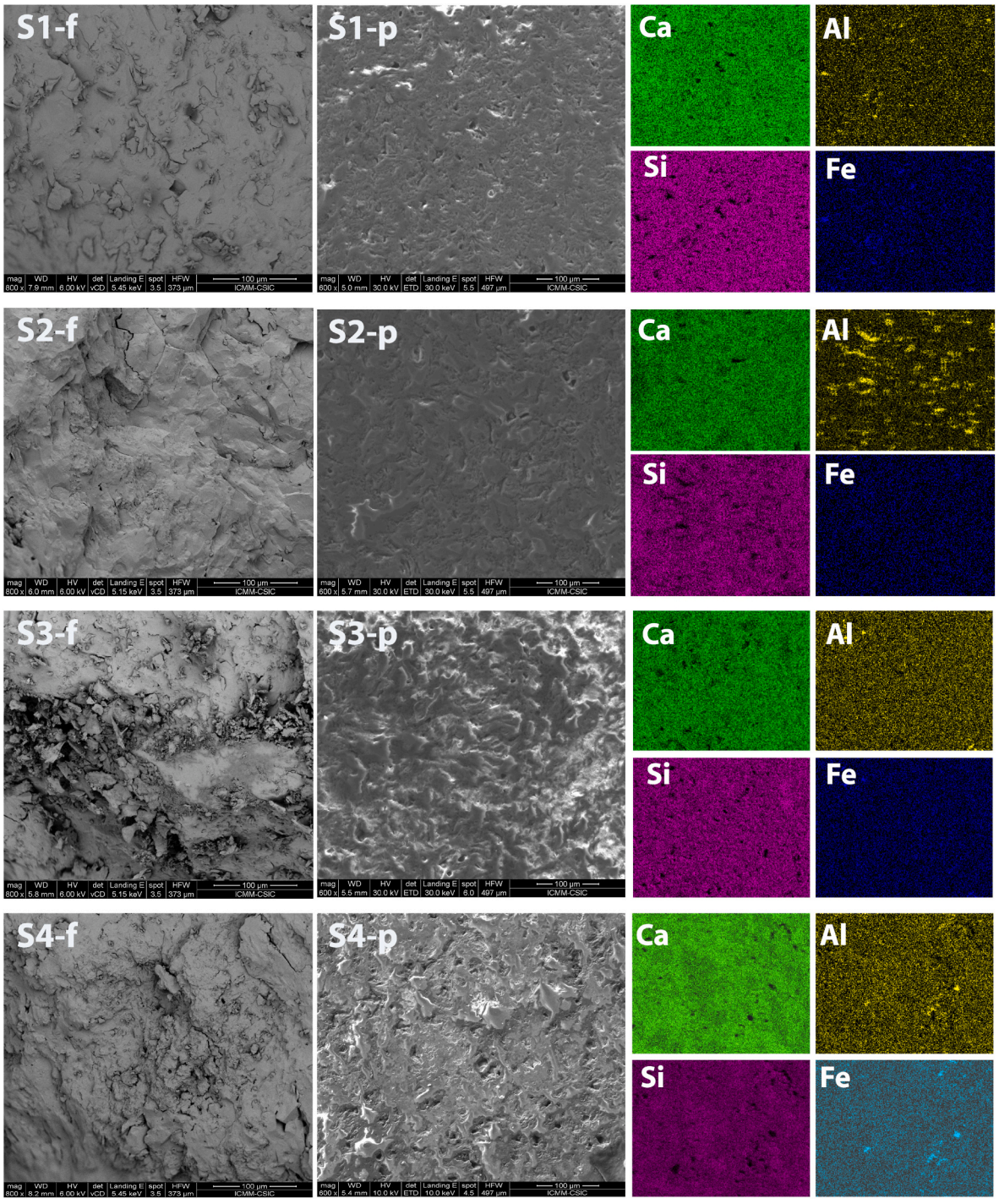

Fig. 3. FE-SEM images of the fresh fracture surfaces (samples labelled with *f*) and polished surfaces (samples labelled with *p*) of every composition. On the right-hand side of the figure, EDX element mapping (Ca, Al, Si, Fe) obtained on the surface of each polished sample.

that all the crystalline calcium silicates have a non-isotropic phase, while garnets have cubic symmetry. It means that, under crossed polarizers, they should appear black through optical microscopy, while anisotropic phases should present some light. In this respect, black areas have been identified by reflectance optical microscopy in samples S1 and S2 (Fig. 5). The use of crossed polarizers ensures that the crystallographic system of the particles in Fig. 5-B is cubic and eliminates the possibility of residual carbon from the Spark Plasma Sintering.

In order to determine the chemical composition, the FESEM-EDX technique has been used (Fig. 5). We have chosen the signals of Ca-Kα, Si-Kα, and Al-Kα to be mapped in blue, red and green, respectively. The fourth image is a composition of these three images over a SEM image of the sample surface. The color composite image shows large areas rich in Al and poor in Si, which have been assigned to calcium aluminates segregated domains (in green color). Moreover, a rich Si stripe runs along the top of the figure. We have identified this region as having a higher garnet concentration. Specifically, this area has been studied by Raman Microscopy.

3.6. Raman microscopy

In this regard, three different types of spectra were recorded. In

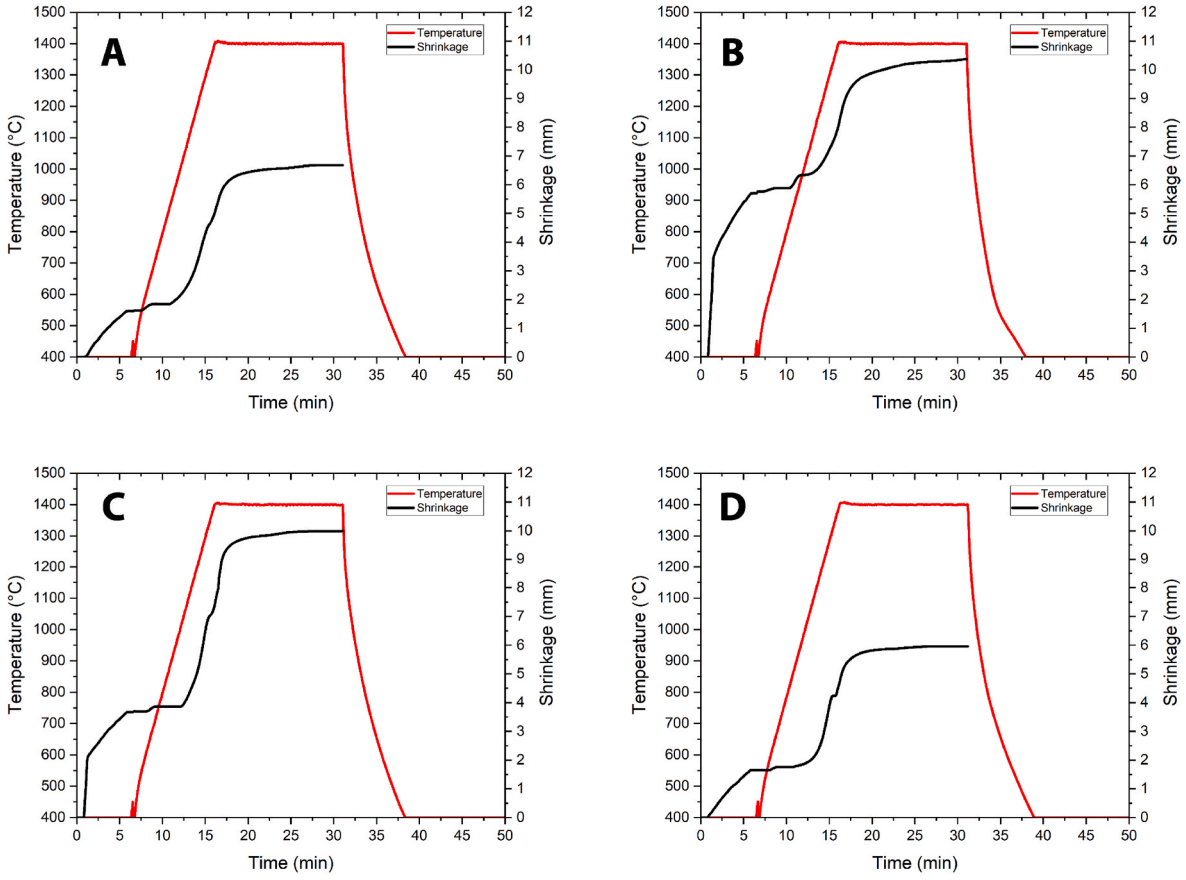

Fig. 4. Sintering curves of: (A) S1, (B) S2, (C) S3, (D) S4 SPSed samples.

Table 2
Measured density, relative density and Vickers hardness of the compacts obtained.

	d (g/cm^3)	d (%)	Hv (GPa)
S1	3.2 ± 0.2	**99.79**	5.4 ± 0.2
S2	3.1 ± 0.1	**94.72**	4.1 ± 0.1
S3	3.1 ± 0.2	**92.34**	3.4 ± 0.3
S4	3.1 ± 0.1	**91.52**	3.6 ± 0.2

Fig. 6, the spectrum of nearly amorphous hartrurite has been plotted in blue (identified by the letter H). As the device approaches the garnet-rich region, new peaks appear, associated with garnet (spectrum labelled as H + G). Finally, in some specific spots, spectra that correspond to almost pure garnet phases (labelled as G) can be seen. It should be noted that the hartrurite and garnet spectra differ sufficiently in Si–O stretching Raman modes to be unambiguously identified, particularly those with frequencies greater than 900 cm^{-1} [39,40].

4. Discussion

In order to understand the processes that occur during spark plasma sintering, we must consider the microstructure of the powder at the beginning of the process into the graphite die. Before applying any current, we have a particle agglomerate mainly constituted by C_3S with variable amounts of C_2S. Regarding the ternary $CaO–SiO_2–Al_2O_3$ phase diagram shown in Fig. 7 [41], if we pay attention to the relative amounts of cations, we can conclude that all the four powders may be located around the region of C_3S but very close to the C_2S primary field.

Taking into account that the SPS heating process is very fast, solid-state diffusion is quite limited. This process is characterized by being carried out with a high heating rate (100 °C/min) and a very short plateau at the maximum temperature. For this reason, thermodynamic equilibrium phases may not be fully achieved and, therefore, it is not surprising that transitory phases appear at the end of the SPS process (i.e., low temperature eutectic/peritectic liquids). Additionally, new phases that do not conform to what the equilibrium diagram predicts at normal conditions may appear, as is certainly the case at hand. Therefore, due to the very high heating and cooling rates, solid state reactions driven by atomic diffusion require times much longer than those allowed by SPS, and, therefore, we can expect that the chemical reactions will only take place in the presence of a liquid phase [42]. Taking into account that clinkers are mainly a mixture of C_3S and C_2S, two different thermodynamic processes must be considered: one for C_2S and a second one for C_3S.

First, according to the calculated phase diagram of the $CaO–Al_2O_3–SiO_2$ system (Fig. 7) [41], above 1308 °C, C_2S decomposes into $C_3S + C_3S_2$, and C_3S_2 quickly decomposes into C_3S + CS, reaching the lowest eutectic point at 1270 °C. If we do not take into account the presence of Al_2O_3 or Fe, we can simplify the reaction as:

$$2C_2S\ (\text{solid}) \rightarrow C_3S\ (\text{solid}) + CS\ (\text{liquid})$$

As a result, almost half of the amount of C_2S becomes liquid and the other half increases the amount of C_3S solid.

On the other hand, the primary crystallization field of C_3S (labelled in Fig. 7 as "*Hat*" for "Hatrurite") presents multiple peritectic points around 1400 °C. In a real SPS cycle, at the plateau temperature of around 1406 °C, we find two immiscible liquid phases corresponding to C_3S and CS. After the holding time, the very fast SPS cooling makes the C_3S magma quickly solidify, while the eutectic liquid CS may remain in such a state as a metastable glassy phase for a longer time. At this point, the amount of C_3S will define the type of structure we are going to find. If

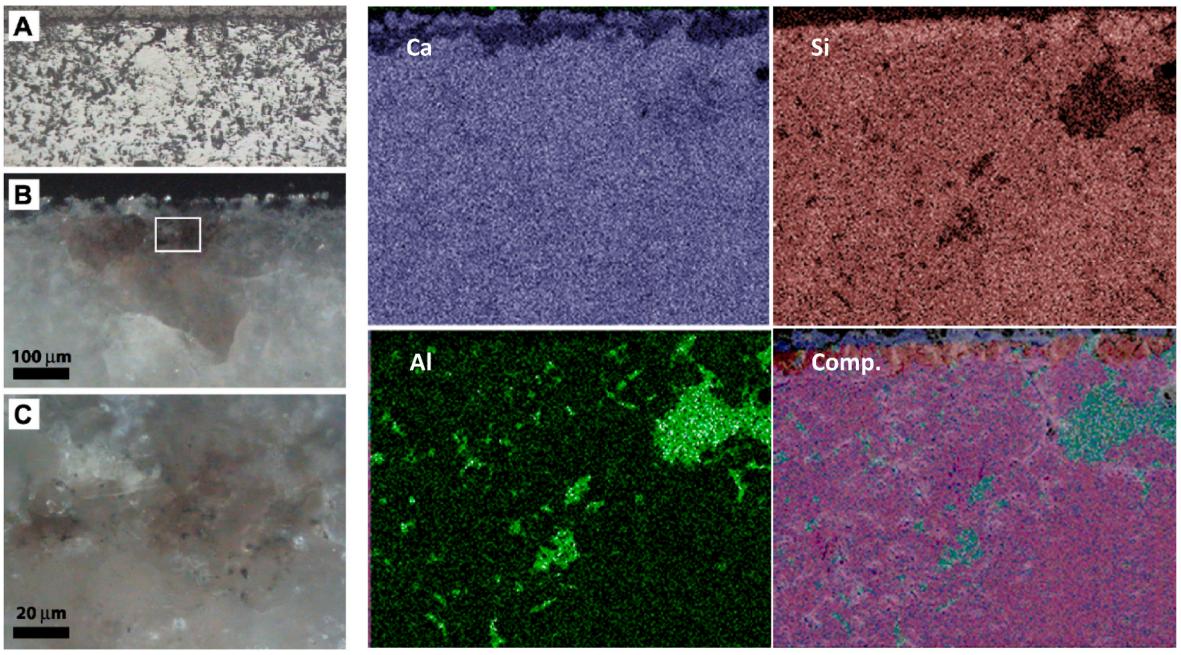

Fig. 5. On the left-hand side of the figure, optical microscope images obtained from polished sample S2 showing: (A) Image obtained under directly transmitted light; (B) image of the same area obtained by observation under crossed polarized light; (C) magnification of the rectangle area indicated in picture (B). Micrograph (B) represents the most common morphology in samples S1 and S2. On the right-hand side of the figure, EDX element mapping (Ca, Si, Al) obtained on the surface of sample S2, and the composition of the three maps on the corresponding SEM image. The rich Si stripe in the upper part corresponds to garnet rich region.

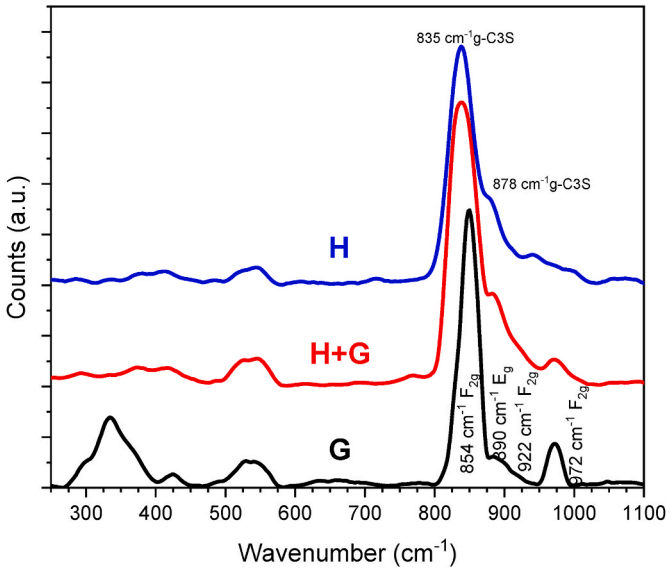

Fig. 6. Raman spectra on different regions of sample 1, showing the presence of Hartrurite (H), a mixture of Hartrurite and Garnet (H + G) and a rich Garnet area (G).

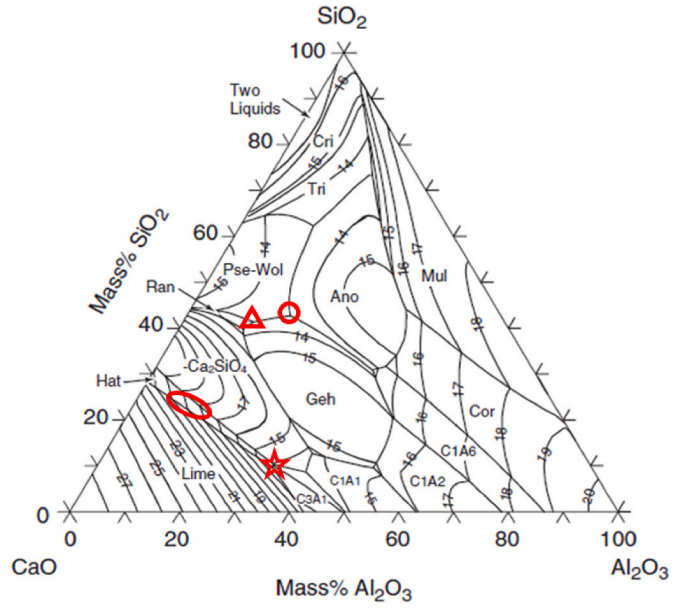

Fig. 7. Calculated phase diagram of the CaO–Al_2O_3–SiO_2 system by Mao et al. from Ref. [41]. The C_3S primary field corresponds to that of *hatrurite* (labelled as "*Hat*"); the C_2S primary field is labelled as *Ca_2SiO_4*. Portland cement compositions are located in the region of the red oval. The eutectic point marked with the circle occurs at 1270 °C. The eutectic point marked with the triangle occurs at 1308 °C. The peritectic reaction marked with a star occurs at 1406 °C. (Ano: anorthite; C_1A_1: CaO·Al_2O_3; C_1A_2: CaO·2Al_2O_3; C_1A_6: CaO·6Al_2O_3; C_3A_1: 3·CaO·Al_2O_3; Cor: corundum; Cri: cristobalite; Geh: gehlenite; Hat: Hatrurite; Mul: mullite; Pse-Wol: pseudo-wollastanite; Ran: rankinite; Tri: tridymite). (For interpretation of the references to color in this figure legend, the reader is referred to the Web version of this article.)

the amount of C_3S is large enough to surround the CS liquid drops, they will stay isolated and entrapped during the cooling process (Fig. 8-A). However, if the C_3S concentration is lower than a specific threshold, liquid will percolate and permeate all over the sample (see Fig. 8-B).

In Fig. 9-A, we have plotted the weight fraction of the main mineralogical components of the powders. In Fig. 9-B, we have plotted the relative concentrations of C_3S and CS in the melt. Taking into account the reaction (1), the [C_3S] and [CS] concentrations at the high temperature regime (HT) can be calculated as:

$$[C_3S]_{HT} = [C_3S]_{pwd} + \tfrac{1}{2}\,[C_2S]_{pwd} \quad (2)$$

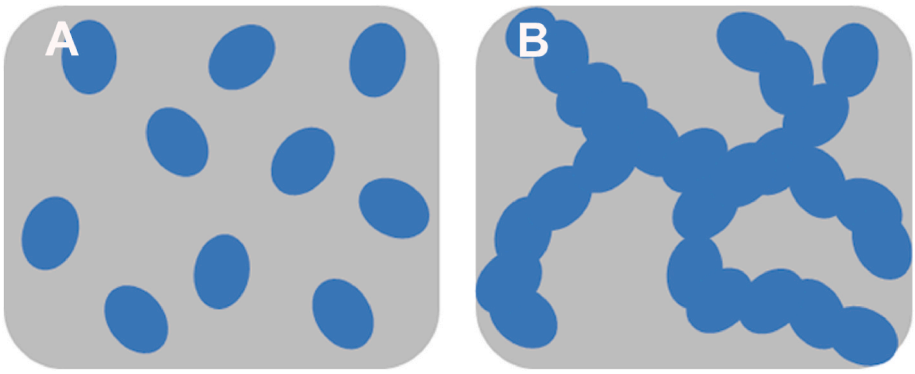

Fig. 8. Schematics of the microstructure of SPSed samples. (A) Solid glass (in grey color) entraps eutectic liquid drops (in blue), corresponding to samples S1 and S2. (B) Solid crystals (grey) have open paths for the percolation of eutectic liquid (blue), corresponding to samples S3 and S4. (For interpretation of the references to color in this figure legend, the reader is referred to the Web version of this article.)

$$[CS]_{HT} = ½\ [C_2S]_{pwd} \quad (3)$$

where *HT* stands for "high T" and *pwd* for "powder". In Fig. 9, it can be seen how samples S1 and S2 have a total amount of $[C_3S]_{HT}$ of around 75%, while for compositions S3 and S4, this value drops below 70%.

As we have mentioned before, in the case of samples S1 and S2, and due to the large concentration of $[C_3S]_{HT}$, the solid magma creates a close structure, trapping drops of the remaining CS liquid. The effect of this phase segregation can be seen in Fig. 5, where areas of calcium aluminate, (CA, green), C_3S (blue) and CS (red) coexist according to EDX. It should be noted that these three components (CA, C_3S and CS) are the products present in the two triple points considered in Fig. 7. For these pictures, we have neglected minority elements, such as Mg, Fe, etc. If we consider it like this, the CS fraction will correspond to the garnet phase. From the image analysis of Fig. 5, and taking into account this "cellular" structure of the melt, one can state that a percolation threshold in the C_3S concentration may exist, above which the liquid migrates/flows through an open pore network (Fig. 8). According to Fig. 9, we estimate that below 75% of C_3S, it completely isolates liquid cavities of CS. We have found a similar situation in rigid and plastic composites, such as the one observed in the case of monoclinic-ZrO_2/Ni composites [43].

Grain growth and crystallization are much more effective in the liquid phase than in the solid. Therefore, in the case that all the liquid phase is confined, as is the case of S1 and S2, grain growth and chemical reactions are hindered, and, consequently, C_3S will stay in a glassy state similar to the melt. The existence of this glassy phase confirms this hypothesis in the XRD diffractograms of S1 and S2 sintered samples, where a broad hump in the baseline is observed for low diffraction angles (Fig. 1).

On the other hand, it should be noted in Fig. 7 how the lowest eutectic temperature has a chemical composition very close to that of garnet (grossular for the herewith treated ternary diagram of phases, and marked with a circle). Therefore, on cooling below 1270 °C, isolated drops of such liquid solidify. As the thermal expansion coefficient of such material is different from that of the matrix, adiabatic thermal stresses should appear in such cavities, which may exceed several GPa as the cooling temperature range is larger than 1000 °C. A simple internal stress calculation, according to the Selsing's model [44,45], has been carried out:

$$P = \frac{\Delta\alpha \cdot \Delta T}{\frac{1+\nu_1}{2E_1} + \frac{1-2\nu_2}{E_2}}$$

where Δα is the difference in thermal expansion, ΔT is the cooling range, E is the modulus of elasticity and ν is the Poisson's ratio. Likewise, subscript 1 refers to the matrix and subscript 2 refers to the isolated cavities. The calculation has been made using the following thermal coefficients (α) and elastic moduli (E) of C_3S and garnet [46,47]: α (C_3S) = $48{\cdot}10^{-6}$ K^{-1}, α (garnet) = $26{\cdot}10^{-6}$ K^{-1}, E (C_3S) = E (garnet) ≅ 160 GPa, ν (C_3S) ≅ 0.2), ν (garnet) = 0.4. The result is that a pressure of up to 6.5 GPa may appear on the CS cavities. Specifically, high pressure is one of the main requisites for the formation of garnets [33,48,49]. In fact, transparent garnet windows have been obtained by high pressure sintering [46]. Moreover, garnets are used in geology as a pressure proxy in the study of rock formation [48]. In this system and for the first time, due to its particular microstructure and chemical composition, it has been possible to obtain garnets by applying quite moderate external pressures (50 MPa) [34]. The highest Vickers hardness values obtained for samples S1 and S2 versus those corresponding to samples S3 and S4 (Table 2) are consistent with the presence of garnet nanoparticles.

Samples S3 and S4 have a smaller fraction of C_3S. As mentioned above, we think that a percolation threshold should exist in this system around 70–75% of [C_3S + ½ C_2S]. For lower C_3S contents, liquid CS phase may flow all along the system inducing a recrystallization, so that the final product is close to the thermodynamic equilibrium, very similar to the initial powders.

One relevant observation that deserves to be pointed out in this work is that artificial sintering routes, such as SPS or hot pressing, have a close resemblance to metamorphic geological processes. In fact, the panoply of different sintering treatments with different ranges of pressure and temperature may reproduce at laboratory level many of the natural rocks found in nature. In particular, SPS has many resemblances to contact metamorphism because of the moderate pressure and high temperatures reached around the graphite die. As clinker powders have a chemical composition that can be found in some natural rocks, the study of the sintered samples may be a model for some specific contact metamorphism events [17,50,51].

In view of these results, we can state that, by choosing selected mixtures of CaO, SiO_2 and trivalent oxides (such as Al_2O_3, Fe_2O_3) as matrix and non-miscible substances, we can obtain materials with unforeseeable morphological changes, specifically by introducing giant local isostatic pressures without large external loads. These results suggest that: i) it will be particularly interesting to study the electrical properties of the materials obtained and find their relationship with their singular morphology, and ii) the giant adiabatic pressures developed in the matrix (>5 GPa) can be used to synthesize superhard nanoparticles i.e. c-BN.

5. Conclusions

In the present work, we have studied a set of different Portland clinker powders after being successfully sintered by Spark Plasma Sintering. Although Portland clinker compositions have a narrow range of variation of calcium silicates, above a critical concentration of calcium,

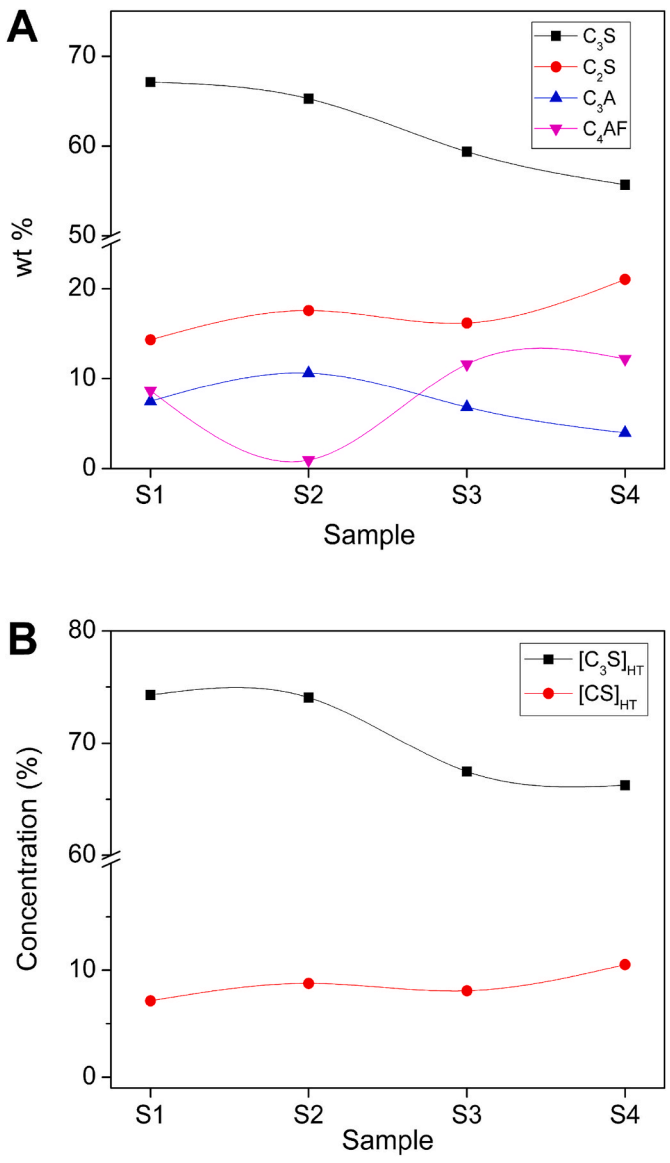

Fig. 9. A) Relative concentration of the different crystalline phases in the four samples of clinker powders. B) The upper line represents the total concentration of C_3S that has appeared from [C_3S+½C_2S] according to equation (2), and the bottom line represents the concentration of CS that has appeared from the melting of [½C_2S] according to equation (3). Notice the large concentration gap between samples S2 and S3.

high-pressure garnets spontaneously appear. A model describing the formation of garnets considering the formation of two transitory eutectic liquids at 1270 °C and 1380 °C has been explained. On cooling, the second liquid, with a composition similar to the C_3S phase, solidifies, entrapping liquid isolated drops, which on fast cooling (>1000 °C), develop high adiabatic thermal stresses of several GPa, inducing the formation of garnets. This artificial sintering SPS route, which has a close resemblance to contact metamorphic geological processes, may be employed to obtain high-pressure phases (GPa) by applying significantly lower pressures (50 MPa).

Declaration of competing interest

The authors declare that they have no known competing financial interests or personal relationships that could have appeared to influence the work reported in this paper.

Acknowledgements

The Authors acknowledge the financial support of the PID2020-119130 GB-I00 project funded by MCIN/AEI/10.13039/501100011033 and by CSIC under grant 201960E103. Thanks to the Official Laboratory for Testing of Construction Materials (LOEMCO, Getafe, Madrid, Spain) for free supply of the clinker samples.

References

[1] J. Stark, Recent advances in the field of cement hydration and microstructure analysis, Cement Concr. Res. 41 (2011) 666–678, https://doi.org/10.1016/J.CEMCONRES.2011.03.028.
[2] D. Wang, C. Shi, N. Farzadnia, Z. Shi, H. Jia, Z. Ou, A review on use of limestone powder in cement-based materials: mechanism, hydration and microstructures, Construct. Build. Mater. 181 (2018) 659–672, https://doi.org/10.1016/J.CONBUILDMAT.2018.06.075.
[3] K. Scrivener, A. Ouzia, P. Juilland, A. Kunhi Mohamed, Advances in understanding cement hydration mechanisms, Cement Concr. Res. 124 (2019), 105823, https://doi.org/10.1016/J.CEMCONRES.2019.105823.
[4] H.-J. Kuzel, H. Baier, Hydration of calcium aluminate cements in the presence of calcium carbonate, Eur. J. Mineral 8 (1996) 129–142, https://doi.org/10.1127/EJM/8/1/0129.
[5] D.A. Kulik, Thermodynamic properties of surface species at the mineral-water interface under hydrothermal conditions: a gibbs energy minimization single-site 2pK(A) triple-layer model of rutile in NaCl electrolyte to 250°C, Geochem. Cosmochim. Acta 64 (2000) 3161–3179, https://doi.org/10.1016/S0016-7037(00)00413-0.
[6] B. Lothenbach, F. Winnefeld, Thermodynamic modelling of the hydration of Portland cement, Cement Concr. Res. 36 (2006) 209–226, https://doi.org/10.1016/J.CEMCONRES.2005.03.001.
[7] T. Matschei, B. Lothenbach, F.P. Glasser, The role of calcium carbonate in cement hydration, Cement Concr. Res. 37 (2007) 551–558, https://doi.org/10.1016/J.CEMCONRES.2006.10.013.
[8] H.J. Kuzel, H. Pöllmann, Hydration of C3A in the presence of Ca(OH)2, CaSO4·2H2O and CaCO3, Cement Concr. Res. 21 (1991) 885–895, https://doi.org/10.1016/0008-8846(91)90183-I.
[9] N. Antón, F. Velasco, E. Gordo, J.M. Torralba, Statistical approach to mechanical behaviour of ceramic matrix composites based on Portland clinker, Ceram. Int. 27 (2001) 391–399, https://doi.org/10.1016/S0272-8842(00)00093-6.
[10] N. Antón, R. Gamboa, V. Amigó, J.M. Torralba, Liquid phase sintering of CMCs based on clinker Portland, J. Eur. Ceram. Soc. 20 (2000) 2215–2224, https://doi.org/10.1016/S0955-2219(00)00069-8.
[11] N. Antón, J.M. Ruiz-Prieto, F. Velasco, J.M. Torralba, Mechanical properties and wear behaviour of ceramic matrix composites based on clinker portland doped with magnesia, J. Mater. Process. Technol. 78 (1998) 12–17, https://doi.org/10.1016/S0924-0136(97)00456-1.
[12] N. Antón, L.E.G. Cambronero, J.M. Ruiz-Prieto, F. Velasco, J.M. Torralba, Ceramic and ceramic matrix composites based on clinker Portland: Sinterability, Key Eng. Mater. 127–131 (1997) 407–414. https://doi.org/10.4028/www.scientific.net/kem.127-131.407.
[13] J.M. Torralba, L.E.G. Cambronero, J.M. Ruiz-Prieto, Using Portland clinker in structural ceramics, Am. Ceram. Soc. Bull. 74 (1995) 90–91.
[14] F. Dunstetter, M.N. De Noirfontaine, M. Courtial, Polymorphism of tricalcium silicate, the major compound of Portland cement clinker: 1. Structural data: review and unified analysis, Cement Concr. Res. 36 (2006) 39–53, https://doi.org/10.1016/j.cemconres.2004.12.003.
[15] C. Naber, F. Goetz-neunhoeffer, M. Göbbels, C. Rößler, J. Neubauer, Cement and Concrete Research Synthesis of monocrystalline Ca 3 SiO 5 using the optical fl oating zone method, Cement Concr. Res. 85 (2016) 156–162.
[16] Z. Gou, J. Chang, W. Zhai, Preparation and characterization of novel bioactive dicalcium silicate ceramics, J. Eur. Ceram. Soc. 25 (2005) 1507–1514, https://doi.org/10.1016/j.jeurceramsoc.2004.05.029.
[17] E.K. Papynov, O.O. Shichalin, I.Y. Buravlev, A.S. Portnyagin, A.A. Belov, V. Y. Maiorov, Y.E. Skurikhina, E.B. Merkulov, V.O. Glavinskaya, A.D. Nomerovskii, A.V. Golub, N.P. Shapkin, Reactive spark plasma synthesis of porous bioceramic wollastonite, Russ. J. Inorg. Chem. 65 (2020) 263–270, https://doi.org/10.1134/S0036023620020138/FIGURES/7.
[18] Z. Tatli, O. Bretcanu, F. Çalışkan, K. Dalgarno, Fabrication of porous apatite-wollastonite glass ceramics using a two steps sintering process, Mater. Today Commun. 30 (2022) 2352–4928, https://doi.org/10.1016/J.MTCOMM.2022.103216.
[19] S.S. Owoeye, S.M. Abegunde, D.O. Folorunso, B.O. Adigun, U. Kingsley, Microstructure, phase and physical evaluation of non-bioactive wollastonite glass – ceramic prepared from waste glass by sintering method, Open Ceram 5 (2021), https://doi.org/10.1016/J.OCERAM.2021.100062.
[20] M. Suarez, A. Fernandez, J.L. Menendez, R. Torrecillas, H.U.J. Hennicke, R. Kirchner, T. Kessel, Challenges and opportunities for spark plasma sintering: a key technology for a new generation of materials, Sinter. Appl. (2013), https://doi.org/10.5772/53706.
[21] E. Fernandez-Garcia, J. Guillem-Marti, C.F. Gutierrez-Gonzalez, A. Fernandez, M. P. Ginebra, S. Lopez-Esteban, Osteoblastic cell response to spark plasma-sintered

zirconia/titanium cermets, J. Biomater. Appl. 29 (2015) 813–823, https://doi.org/10.1177/0885328214547400.
[22] I. Alvarez-Clemares, G. Mata-Osoro, A. Fernández, S. Lopez-Esteban, C. Pecharroman, R. Torrecillas, J.S. Moya, Ceria doped alumina by Spark Plasma Sintering for optical applications, J. Eur. Ceram. Soc. 32 (2012) 2917–2924, https://doi.org/10.1016/J.JEURCERAMSOC.2012.02.037.
[23] C.F. Gutierrez-Gonzalez, S. Agouram, R. Torrecillas, J.S. Moya, S. Lopez-Esteban, Ceramic/metal nanocomposites by lyophilization: spark plasma sintering and hardness, Ceram. Int. 40 (2014) 4135–4140, https://doi.org/10.1016/J.CERAMINT.2013.08.068.
[24] Y. Makino, K. Mizuuchi, M. Tokita, Y. Agari, M. Kawahara, K. Inoue, Synthesis of new structural and functional materials by SPS processing, Mater. Sci. Forum (2010) 2091–2096, https://doi.org/10.4028/WWW.SCIENTIFIC.NET/MSF.638-642.2091, 638–642.
[25] O.O. Shichalin, I.Y. Buravlev, E.K. Papynov, A.V. Golub, A.A. Belov, A. A. Buravleva, V.N. Sakhnevich, M.I. Dvornik, N.M. Vlasova, A.V. Gerasimenko, V. P. Reva, A.A. Yudakov, Comparative study of WC-based hard alloys fabrication via spark plasma sintering using Co, Fe, Ni, Cr, and Ti binders, Int. J. Refract. Met. Hard Mater. 102 (2022), 105725, https://doi.org/10.1016/J.IJRMHM.2021.105725.
[26] C. Pecharromán, J.E. Iglesias, Effective dielectric properties of packed mixtures of insulator particles, Phys. Rev. B 49 (1994) 7137–7147, https://doi.org/10.1103/PhysRevB.49.7137.
[27] C. Pecharroman, J.E. Iglesias, A method for the determination of infrared optical constants from reflectance measurements on powdered samples, J. Phys. Condens. Matter 6 (1994) 7125–7141, https://doi.org/10.1088/0953-8984/6/35/021.
[28] C. Pecharromán, M. Ocaña, C.J. Sema, Optical constants of tetragonal and cubic zirconias in the infrared, J. Appl. Phys. 80 (1996) 3479–3483, https://doi.org/10.1063/1.363218.
[29] J.E.F.S. Rodrigues, M.M. Ferrer, M.L. Moreira, J.R. Sambrano, R.C. Costa, A. D. Rodrigues, P.S. Pizani, Y. Huttel, J.A. Alonso, C. Pecharromán, Unveiling the infrared complex dielectric function of ilmenite CdTiO3</inf&gt, J. Alloys Compd. 813 (2020), https://doi.org/10.1016/j.jallcom.2019.152136.
[30] C. Pecharromàn, J.E. Iglesias, Modeling particle size and clumping effects in the IR absorbance spectra of dilute powders, Appl. Spectrosc. 50 (1996) 1553–1562, https://doi.org/10.1366/0003702963904539.
[31] E.F. Baxter, M.J. Caddick, J.J. Ague, Garnet: common mineral, uncommonly useful, Elements 9 (2013) 415–419, https://doi.org/10.2113/gselements.9.6.415.
[32] Y. Wang, Q. Sun, D. Duan, X. Liu, X. Bao, The study of crystal structure on grossular–andradite solid solution, Minerals 9 (2019), https://doi.org/10.3390/min9110691.
[33] N. Sibi, G. Subodh, Structural and microstructural correlations of physical properties in natural almandine-pyrope solid solution: Al70Py29, J. Electron. Mater. 46 (2017) 6947–6956, https://doi.org/10.1007/s11664-017-5801-5.
[34] D.S. Coombs, Y. Kawachi, B.F. Houghton, G. Hyden, I.J. Pringle, J.G. Williams, Andradite and andradite-grossular solid solutions in very low-grade regionally metamorphosed rocks in Southern New Zealand, Contrib. Mineral. Petrol. 63 (1977) 229–246, https://doi.org/10.1007/BF00375574.
[35] X. Ren, W. Zhang, J. Ye, FTIR study on the polymorphic structure of tricalcium silicate, Cement Concr. Res. 99 (2017) 129–136, https://doi.org/10.1016/j.cemconres.2016.11.021.
[36] M. Martín-Garrido, S. Martínez-Ramírez, G. Pérez, A. Guerrero, Calcium silicate hydrate characterization by spectroscopic techniques, V Conf. Int. YOCOCU 21 (2016) 1–5. Al 23 Septiembre 2016.
[37] S.P. Varma, E. Henderson, C.D. Wall, The application of low temperature infra-red spectroscopy to studies of iron substitution in tricalcium aluminate (C3A), Cement Concr. Res. 11 (1981) 211–218, https://doi.org/10.1016/0008-8846(81)90062-4.
[38] D.L. Whitney, M. Broz, R.F. Cook, Hardness, toughness, and modulus of some common metamorphic minerals, Am. Mineral. 92 (2007) 281–288, https://doi.org/10.2138/AM.2007.2212.
[39] B.A. Kolesov, C.A. Geiger, Raman spectra of silicate garnets, Phys. Chem. Miner. 25 (1998) 142–151, https://doi.org/10.1007/S002690050097.
[40] S. Martinez-Ramirez, M. Frías, C. Domingo, Micro-Raman spectroscopy in white portland cement hydration: long-term study at room temperature, J. Raman Spectrosc. 37 (2006) 555–561, https://doi.org/10.1002/JRS.1428.
[41] H. Mao, M. Hillert, M. Selleby, B. Sundman, Thermodynamic assessment of the CaO-Al2O3-SiO 2 system, J. Am. Ceram. Soc. 89 (2006) 298–308, https://doi.org/10.1111/J.1551-2916.2005.00698.X.
[42] J.A. Pask, A.P. Tomsia, Wetting, spreading and reactions at liquid/solid interfaces, Mater. Sci. Res. 14 (1981) 411–419, https://doi.org/10.1007/978-1-4684-3947-2_36.
[43] J.S. Moya, S. López-Esteban, C. Pecharromán, J.F. Bartolomé, R. Torrecillas, Mechanically stable monoclinic zirconia-nickel composite, J. Am. Ceram. Soc. 85 (2002) 2119–2121, https://doi.org/10.1111/J.1151-2916.2002.TB00416.X.
[44] J. Selsing, Internal stresses in ceramics, J. Am. Ceram. Soc. 44 (1961), https://doi.org/10.1111/J.1151-2916.1961.TB15475.X, 419–419.
[45] D. Perkins, E.J. Essene, E.F. Westrum, V.J. Wall, Application of new thermodynamic data to grossular phase relations, Contrib. Mineral. Petrol. 64 (1977) 137–147, https://doi.org/10.1007/BF00371508, 1977 642.
[46] (PDF) Changes in the cell parameters of alite doped with phosphorus. https://www.researchgate.net/publication/279916727_Changes_in_the_cell_parameters_of_alite_doped_with_phosphorus. (Accessed 23 June 2022).
[47] D.G. Isaak, O.L. Anderson, H. Oda, High-temperature thermal expansion and elasticity of calcium-rich garnets, Phys. Chem. Miner. 19 (1992) 106–120, https://doi.org/10.1007/BF00198608, 1992 192.
[48] W. Du, X. Li, B. Li, Microstrain in pyrope-grossular garnet solid solution at high pressure: a case study of Py90Gr10 and Py10Gr90 up to 15 GPa, Phys. Chem. Miner. 44 (2017) 377–388, https://doi.org/10.1007/s00269-016-0865-y.
[49] T. Irifune, K. Kawakami, T. Arimoto, H. Ohfuji, T. Kunimoto, T. Shinmei, Pressure-induced nano-crystallization of silicate garnets from glass, Nat. Commun. 7 (2016) 1–7, https://doi.org/10.1038/ncomms13753.
[50] O.O. Shichalin, E.K. Papynov, V.Y. Maiorov, A.A. Belov, E.B. Modin, I.Y. Buravlev, Y.A. Azarova, A.V. Golub, E.A. Gridasova, A.E. Sukhorada, I.G. Tananaev, V. A. Avramenko, Spark plasma sintering of aluminosilicate ceramic matrices for immobilization of cesium radionuclides, Radiochemistry (Moscow, Russ. Fed.) 61 (2019) 185–191, https://doi.org/10.1134/S1066362219020097, 2019 612.
[51] E.K. Papynov, O.O. Shichalin, A.Y. Mironenko, A.V. Ryakov, I.V. Manakov, P. V. Makhrov, I.Y. Buravlev, I.G. Tananaev, V.A. Avramenko, V.I. Sergienko, Synthesis of high-density pellets of uranium dioxide by spark plasma sintering in dies of different types, Radiochemistry (Moscow, Russ. Fed.) 60 (2018) 362–370, https://doi.org/10.1134/S1066362218040045, 2018 604.